nature geoscience

Article

https://doi.org/10.1038/s41561-023-01138-x

Rapid night-time nanoparticle growth in Delhi driven by biomass-burning emissions

Received: 7 July 2022

Accepted: 26 January 2023

A list of authors and their affiliations appears at the end of the paper

Natural and anthropogenic biomass burning are among the major sources of particulate pollution worldwide that affects air quality, climate and human health. Delhi, one of the world's most populated cities, experiences severe haze events caused by particulate pollution during winter, but the underlying pathways remain poorly understood. Here we observe intense and frequent nocturnal particle growth events during haze development in Delhi from measurements of aerosols and gases during January–February at the Indian Institute of Technology in Delhi. The particle growth events occur systematically despite the unfavourable condition for new-particle formation, including the lack of photochemical production of low-volatility vapours and considerable loss of vapours under extremely polluted conditions. We estimate that this process is responsible for 70% of the total particle-number concentration during haze. We identify that the condensation of primary organic vapours from biomass burning is the leading cause of the observed growth. The sharp decrease in night-time temperatures and rapid increase in biomass-burning emissions drive these primary organic vapours out of equilibrium, resulting in their condensation and the growth of nanoparticles into sizes relevant for haze formation. This high impact of primary biomass-burning emissions on night-time nanoparticle growth is unique compared with most urban locations globally, where low-volatility vapours formed through oxidation during the day drive particle growth and haze formation. As uncontrolled biomass burning for residential heating and cooking is rife in the Indo–Gangetic plain, we expect this growth mechanism to be a source of ultrafine particles, affecting the health of 5% of the world's population and impacting the regional climate. Our work implies that regulating uncontrolled biomass-combustion emissions may help inhibit nocturnal haze formation and improve human health in India.

Air pollution is responsible for 18% of the total annual premature deaths in India[1]. New Delhi, which lies in the Indo–Gangetic Plain (IGP), has been ranked the world's most polluted capital for the past three years[1], with particulate matter (PM) levels of more than 500 $\mu g\ m^{-3}$ during winter[2]. Widespread anthropogenic emissions over the IGP result in the formation of winter haze under conducive weather conditions, especially during the night[3,4].

New-particle formation (NPF)[5] and growth events have been recently suggested to be linked to haze formation in highly polluted urban environments[6], for example, in Beijing[7]. These events are generally observed during the day[8], driven mainly by the nucleation of H_2SO_4 from SO_2 photo-oxidation followed by the growth of the newly formed particles into sizes relevant to haze. The drivers of nocturnal haze formation in Delhi remain much less understood. Because of the low

e-mail: snt@iitk.ac.in; imad.el-haddad@psi.ch; andre.prevot@psi.ch

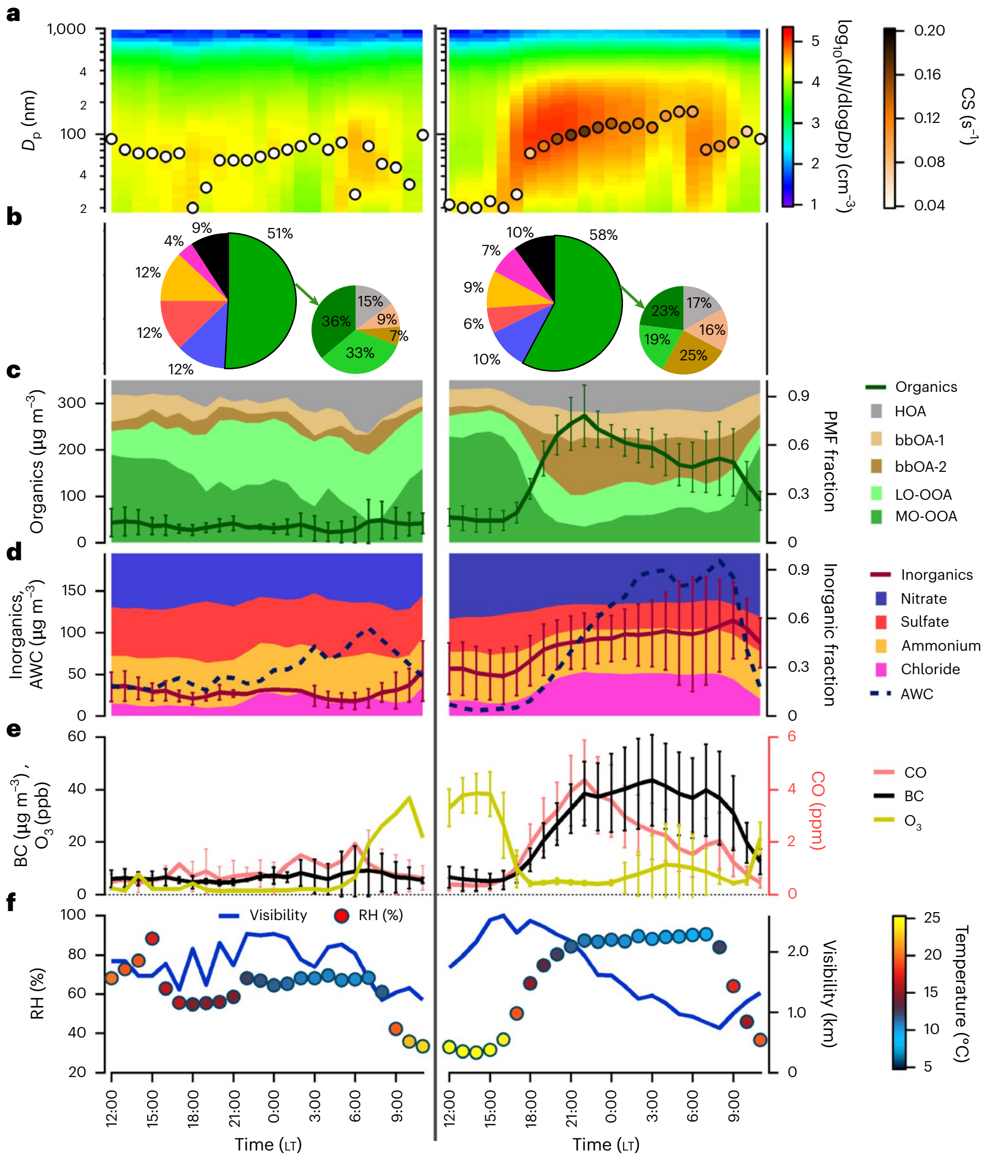

Fig. 1 | The phenomenology of non-NPG and NPG events. a–f, Averaged diel variation of particle-number–size distributions and particle mode diameter colour coded with CS (**a**), fractional contributions to total PM$_1$ and organic factors alone (**b**), organics (the line and the error bars represent the mean ± 1 s.d.) (dark green line) and stacked organic factors (colour shaded) (**c**), total inorganics (the line and the error bars represent the mean ± 1 s.d.) and AWC (left *y* axis) and stacked AMS (nitrate, sulfate, ammonium and chloride) fractions (right *y* axis) (**d**), BC (the line and the error bars represent the mean ± 1 s.d.) and ozone (left *y* axis) and carbon monoxide (right *y* axis) (**e**) and RH (left *y* axis), visibility and temperature (colour-coded filled circles) (**f**) for non-NPG days (left side; $n = 2$) and NPG days (right side; $n = 9$). The solar radiation increases from 7:00 LT and reduces from 16:00 LT. D_p, particle diameter; dN, particle number concentration.

production rates of H_2SO_4 during the night, nocturnal NPF and growth events are generally less frequently observed in urban environments[9]. Therefore, nocturnal haze has been expected to be driven by direct particle emissions. There is only a limited number of NPF and growth studies in India[10,11], none of which reports nocturnal NPF and growth during intense haze formation.

Recent ambient observations of particle-phase composition[12,13] highlighted the elevated chloride concentrations in Delhi, suggesting that the partitioning of chloridric acid may sustain growth under low-ambient-temperature and high-relative-humidity conditions during nocturnal haze in Delhi[14]. However, it is unknown whether ammonium chloride (NH_4Cl) formation can contribute to the growth of nanoparticles during the night. Meanwhile, widespread agricultural-residue burning at the onset of winter and local burning of biomass, trash and solid waste[15] are also important regional pollution sources[16] of directly emitted primary organic aerosols[17] (OAs) and oxygenated OA (OOA) precursors[18,19]. Laboratory and modelling studies have shown that these precursors can rapidly form OOAs under dark conditions when exposed to nitrogen dioxide (NO_2) and ozone (precursors of NO_3)[20,21]. However, how important night-time chemistry is for nocturnal particle pollution in Delhi remains unknown, especially with the high night-time concentrations of NO and organic vapours, which effectively scavenge NO_3 radicals. Therefore, the most important sources and processes involved in nocturnal haze formation in Delhi remain unknown.

In this Article, through intensive wintertime field measurements in Delhi, we provide direct observational evidence and a mechanistic understanding of nocturnal growth of nanoparticles during haze formation. We show that primary organic vapours emitted from biomass burning are the major driver of early particle growth through rapid condensation under favourable atmospheric conditions.

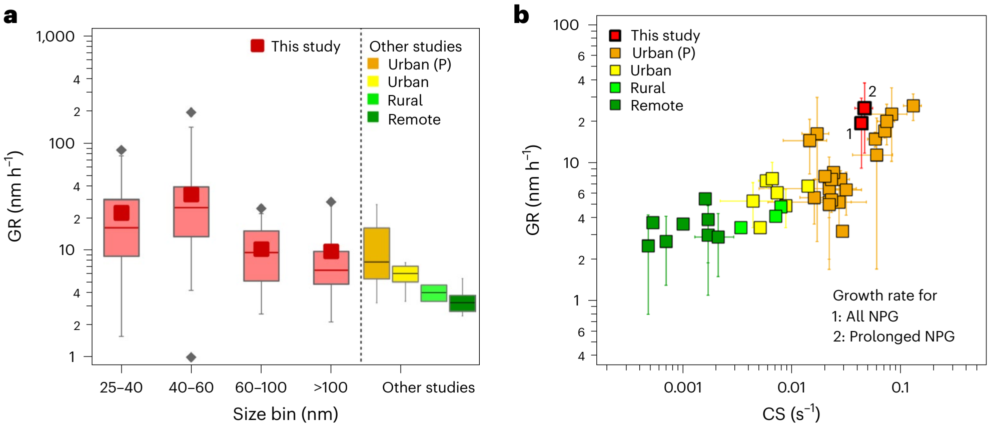

Fig. 2 | Growth-rate observations and their comparison with other reported values across the world. a, Box-and-whisker plots of size-resolved growth rates for all the growth events ($n = 27$) from SMPS (in size bins 25–40 nm, 40–60 nm, 60–100 nm and >100 nm) along with the growth rates reported from other environments from the world (the urban polluted regions (Urban (P)) are distinguished by high condensation-sink values) (Supplementary Table 4). The bottom and top of each box indicate 25th and 75th percentiles, respectively; the top and bottom of each whisker indicate the 5th and 95th percentiles. The horizontal line within each box indicates the median; the red coloured square symbol indicates the arithmetic mean. **b**, GR versus CS variation of the same ($n = 39$). The square boxes and the error bars represent the mean ± 1 s.d.

Nocturnal particle growth during haze formation in Delhi

Intensive ambient measurements of aerosol physical and chemical properties using state-of-the-art instrumentation were conducted during January–February 2019 at the Indian Institute of Technology (IITD), Delhi, India (Methods). At IITD, out of the 33 nights of the measurement period, we observed rapid particle growth events on 27 nights. We refer to these as nocturnal particle growth (NPG) events. Out of these 27 NPG events, 9 showed prolonged growth extending up to noon the next day.

Figure 1 illustrates the evolution of particle size and chemical composition during these nine prolonged NPG events and contrasts it with days when no NPG was observed (non-event days). During NPG events, high growth rates ranging between 9 and 55 nm h^{-1} were observed in the 20–100 nm size range in the early evening (Fig. 1a and Extended Data Fig. 1). These figures show that the aerosol concentrations before growth are similar during NPG and non-NPG days. Extended Data Fig. 2 is related to the average of 27 NPG days whereas the top right panel of Fig. 1 relates to the average of 9 strong NPG events that occur throughout the night and are extended up to noon the next day. The particle-number mode diameter increased from 19 to 70 nm between 16:00 and 18:00 LT and continued to increase slowly past midnight. During growth, the submicron aerosol mass loadings increased from ~200 μg m^{-3} to ~400 μg m^{-3} between 18:00 and 22:00 LT (Fig. 1b–d). During this period, a similar increase was observed in the concentrations of primary pollutants, for example, carbon monoxide (CO) from 0.3 to 4.2 ppm and black carbon (BC) from 4 to 44 μg m^{-3} (Fig. 1e). Mass concentrations of PM of less than 1 μm diameter in size (PM_1) were 269 ± 122 μg m^{-3} on the NPG days compared with 72 ± 13 μg m^{-3} for non-event days (24 h average). The NPG days also show four to five times higher particle-number concentrations (Extended Data Fig. 3 and Supplementary Text 1). Through parallel measurements conducted at a suburban site ~20 km downwind from IITD, we show that these NPG events are not local phenomena but occur in the wider area of Delhi (Extended Data Fig. 4). The nocturnal growth is supported by conducive atmospheric conditions, favouring a rapid drop in temperature from 25 °C to 5 °C and an increase in relative humidity (RH) from 40% to 90% (Fig. 1f).

Size-resolved growth rates (ss-GRs) were calculated for all the events for the size bins 25–40 nm, 40–60 nm, 60–100 nm and >100 nm. The highest GR was observed at 40–60 nm (33.2 ± 35.9 nm h^{-1}), followed by 20–40 nm (22.3 ± 19.4 nm h^{-1}), 60–100 nm (10.3 ± 5.7 nm h^{-1}) and >100 nm (9.8 ± 7.4 nm h^{-1}) (Fig. 2a). The prolonged NPG events showed substantially higher growth rates for the particles in the range of 25–60 nm (GR_{25-60} = 40 nm h^{-1}) compared with the total average of all NPG (GR_{25-60} = 28 nm h^{-1}) (Supplementary Table 1). The values are presented in Fig. 2b, along with the variations and comparisons with other reported values in different environments worldwide. GRs are at the high end of what has been reported in polluted urban environments across the world; for example, they are three to four times higher than in wintertime in Beijing[22]. The condensation sink (CS)—particles acting as a sink of newly formed particles and condensable vapours (measured per second)—is comparatively high in Delhi. Despite this high CS[23,24], the GR remained extremely high, indicating that the emission or production rates of the condensable vapours are critical.

Aerosol composition and sources during haze

Figure 1b shows the particle chemical composition during event and non-event days. Organics accounted for about 58% of the total PM_1 mass during NPG events, while the remainder is composed of inorganics and BC. The OA concentrations show the most important increase during the events (by a factor of five), followed by chloride and nitrate (Fig. 1c,d). The highest organic mass concentration is observed at 22:00 LT, concurrent with the highest PM_1 mass concentrations. The inorganic fraction increases by a factor of two throughout the night during the NPG events. Sulfate concentrations remain almost constant during the events and contribute on average 11% to the total inorganic fraction. While nitrate was the most important inorganic component on average (37% of the inorganics), chloride showed the sharpest increase during the event days (from 8% to 27% of the inorganics). The fraction of ammonium nitrate was higher before the event, while NH_4Cl dominated as the temperature dropped and the RH increased. The primary enhancement in the inorganic fraction mass concentration can be attributed to NH_4Cl. Unlike the organic fraction, NH_4Cl concentrations continued to rise throughout the night, which, together with the increase in relative humidity, resulted in an increase in the aerosol liquid-water content (AWC) from 20 μg m^{-3} to 190 μg m^{-3}. This is consistent with the findings in ref. [14], indicating that such high AWC offers an aqueous medium into which additional NH_4Cl can partition.

Positive matrix factorization (PMF; Methods) was performed on the high-resolution time-of-flight aerosol mass spectrometer (HR-ToF-AMS; Methods) data to identify and quantify the sources of organics. PMF analysis resulted in five identifiable factors (Fig. 1b):

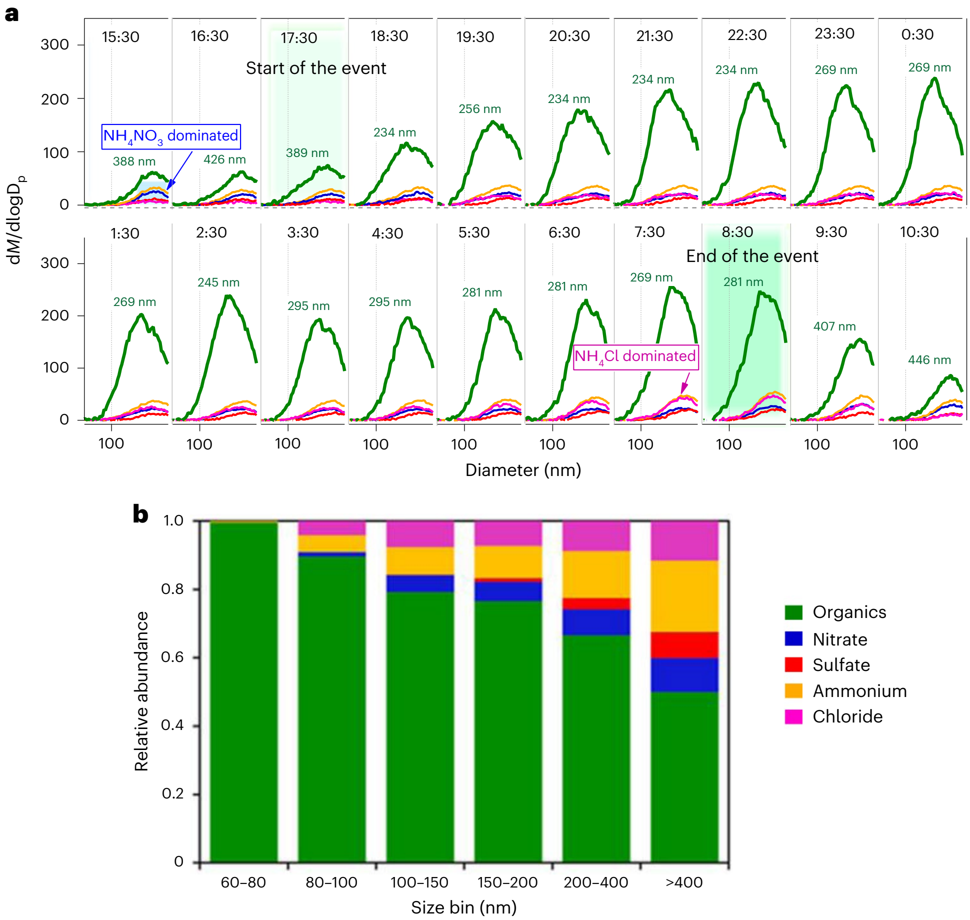

Fig. 3 | Size-resolved chemical speciation during nocturnal growth days. **a**, The evolution of the hourly averaged mass–size distributions of organic and inorganic species with a gap of one hour during nocturnal growth events observed on 16 January 2019. **b**, Relative contributions of organics, nitrate, sulfate, ammonium and chloride in different size bins from 60 nm to 1,000 nm for all NPG days.

hydrocarbon-like OA (HOA) related to traffic, two biomass-burning OA (bbOA) factors, bbOA-1 and bbOA-2, and two OOA factors, less-oxidized OOA (LO-OOA) and more-oxidized OOA (MO-OOA) (Extended Data Fig. 5a and Supplementary Text 2). The HOA factor exhibits high contributions from C_xH_y fragments ($C_3H_5^+$, $C_3H_7^+$, $C_4H_7^+$ and $C_3H_9^+$) related to hydrocarbon fragmentation. Both bbOA factors are characterized by high contributions from *m*/*z* 60 ($C_2H_4O_2^+$) and *m*/*z* 73 ($C_3H_5O_2^+$) from the fragmentation of cellulose pyrolysis products (for example, levoglucosan)[25]. These fragments have a higher contribution in bbOA-2, while bbOA-1 is comparatively more rich in oxidized fragments, probably indicative of more aged emissions (Extended Data Fig. 5b). Another distinctive feature between these two factors is that, while bbOA-1 increases by a factor of ~2–3 during the night, bbOA-2 increases by a factor of ~10. Among the two oxygenated factors, MO-OOA is more oxygenated than LO-OOA, with a bulk O/C ratio of ~1. On average, during the study period, the OOAs were the most important contributors to the total OA mass (47%) (Extended Data Fig. 6a,b), while during the NPG events, bbOA dominated (Extended Data Fig. 6c). Among the OA factors, bbOA-2 showed the most considerable increase during the NPG days (Extended Data Fig. 7a,b). This is in stark contrast with NPF and growth events observed across the globe in general, and in Beijing in particular, where growth follows mainly an increase of the secondary fraction of the aerosol[26].

Mechanistic understanding of particle growth

In Fig. 3a, we examine the chemically resolved mass–size distributions from HR-ToF-AMS measurements for a typical NPG event (16 January 2019). As the concentration of the organics increased five times compared with the values right before the growth event, their size mode shifts from 426 nm to comparatively smaller sizes of 234 nm. The inorganic species also showed an important increase throughout the night. However, this fraction, including NH_4Cl, was in the accumulation mode, and the growing sub-100 nm particles were composed of organics only. This is clearly illustrated in Fig. 3b, showing that 60–80 and 80–100 nm particles were 99% and 90% composed of organics, respectively. By contrast, the organic contribution decreased to only 50% for 400 nm particles, replaced by NH_4Cl that contributed to 32.5% in this size range. Thus, the smaller growing particles consisted entirely of organics, while the NH_4Cl was found in larger particles, which suggests that NH_4Cl is probably less involved in early particle growth. By contrast, NH_4Cl appeared to form by condensation of HCl and NH_3 onto the electrolyte-rich accumulation-mode particles where most of the aerosol water resided. In addition, while the enhancement of the organic concentration coincided with the growth of small particles early in the evening, the NH_4Cl formation appeared to sustain the growth of larger particles later in the night when the low temperature and high RH and liquid-water content promoted the partitioning of HCl and NH_3 (ref. [27]). We calculated the growth rates of single components from the chemically resolved mass–size distributions measured by the HR-ToF-AMS and compared them with the growth rates of the overall aerosol size distributions measured by the scanning mobility particle sizer (SMPS). Only the growth in the size distribution of the organic fraction notably correlates with the particle growth rates (Extended Data Fig. 8a,b) (Pearson's *R*: 0.51, *P* = 0.02), while the inorganic fractions

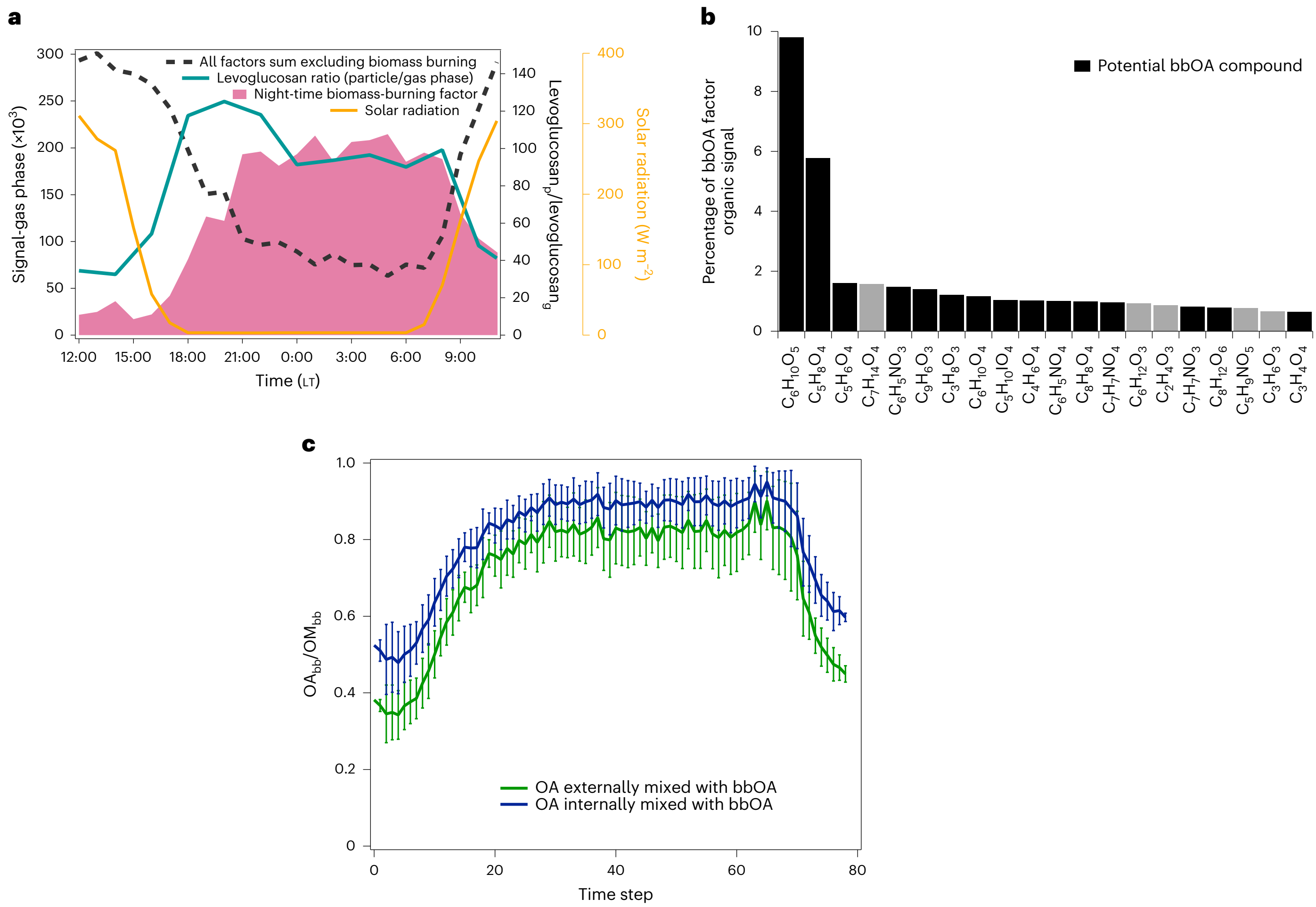

Fig. 4 | Identification of the potential pathway for nocturnal particle growth from the gas-phase composition. a, The time evolution of the gas-phase factors from FIGAERO-CIMS along with the ratio of the particulate and gaseous phases of bbOA for nocturnal growth event and the solar radiation. **b**, Chemical compound information of the night-time biomass-burning factor. **c**, Ratio between the measured OA concentrations from biomass burning (OA_{bb}) and total organic material from biomass burning (OM_{bb}) (as retrieved from box-modelling thermodynamic partitioning calculation and assuming bbOA to be internally and externally mixed with OA) for the NPG events. Each time step indicates a 15 min time span from 16:00 LT to 12:00 LT the next day (*n* = 9 d). The errors constitute uncertainties on the bbOA mixing state with the other organics. The line and the error bars represent the mean ± 1 s.d.

show insignificant correlation (Extended Data Fig. 8c), indicating the dominance of the organics in growth. Overall, both the timing of the increase in the NH_4Cl and OA concentrations and their size distributions strongly suggest that the organics govern the sub-100 nm particle growth during the first hours of the growth events, while NH_4Cl sustains the growth of accumulation-mode particles in the evening. The main contributor to the organic fraction showing a stark increase during early particle growth is bbOA-2, together with bbOA-1 and LO-OOA (Extended Data Fig. 7). In the following, we further investigate the growth process by organic vapours.

To identify the sources of condensing organic vapours during early particle growth, PMF was performed on the gas-phase measurements obtained from the filter inlet for gases and aerosols chemical ionization mass spectrometer (FIGAERO-CIMS). A six-factor solution was found to represent the data well (Fig. 4a and Supplementary Text 3). Only one factor, which was identified to be related to night-time biomass burning, peaks during night-time. All others do not as they exhibit a strong decreasing trend. This factor is dominated by key markers of biomass smoke such as anhydrous sugars ($C_6H_{10}O_5$) from the pyrolysis of cellulose, nitro-catechol ($C_6H_5NO_4$), nitro-phenol ($C_6H_5NO_3$) and others ($C_5H_6O_4$, $C_3H_8O_3$, $C_5H_8O_4$) (Fig. 4b). We note that the high levels of NO (~200–300 ppb) and organic vapours probably scavenged both O_3 and NO_3 radicals, which inhibited the nocturnal oxidation of biomass smoke under our conditions and may explain the low contribution of secondary vapours in the night. The enhancement in the biomass-burning factor coincided remarkably well with the early growth observed in the particle phase (Fig. 4a). While this factor contributed on average ~30% to the signals of total vapours measured by FIGAERO-CIMS, its contribution increased to ~70% during the NPG events (Extended Data Fig. 9a,b). This indicates that biomass-burning vapours are prominently present during NPG events and may play a key role in growth.

Anhydrous sugars were also measured in the particle phase by FIGAERO-CIMS. The diel cycle of the particle-phase signals followed the concentrations of bbOA-2, increasing more than fourfold during the NPG events (Extended Data Fig. 9c). These biomass-burning combustion products showed enhanced gas-to-particle partitioning[28] during early growth as their fraction in the particle phase with respect to the gas phase increased more than threefold (Fig. 4a). Thus, the enhanced partitioning of primary biomass-burning vapours into the particle phase indicates they may contribute to nanoparticle growth during the nocturnal haze events in Delhi. We estimate the contribution of these primary vapours to early particle growth.

To contribute to particle growth, biomass-burning vapours are required to be supersaturated compared with the particle phase. In view of the strong drop in temperature and the rapid increase in primary biomass-burning emissions during haze formation, we expect biomass emissions not to equilibrate, but rather approach a modest steady-state supersaturation that drives the condensation of vapours to balance their emissions and the decrease in their saturation vapour pressures. In this Article, we examine whether the condensation of primary supersaturated biomass-burning vapours can explain the observed growth. We used thermodynamic modelling to estimate the extent to which the partitioning of biomass-burning vapours contributed to the enhancement in the OA mass concentrations[29]. In this model application, which is based on the volatility basis set, the effects of relative humidity, temperature, concentrations and the mixing state of the primary bbOA fraction with the other OA components are considered. The potential effect of atmospheric ageing on the formation of additional low-volatility compounds capable of partitioning into the particle phase was not accounted for. In Fig. 4c, the modelling results are shown for both internally and externally mixed bbOA. The resulting simulations suggest that the fraction of biomass-burning species in the particle phase is enhanced from 50% to 80% during the early growth period, that is, ~40%, or 44 µg m^{-3}, of total bbOA was due to the condensation of semi-volatile vapours (Fig. 4c). This partitioning enhancement was due primarily to the decrease in the vapour pressure of biomass-burning compounds with the decrease in temperature from ~25 °C to ~5 °C, to the increase in the absorptive organic mass concentration and, to a lesser extent, to the increase in RH from 40% to 90% (Fig. 1f). Modelling results are consistent with the enhanced partitioning of anhydrous sugars observed by our FIGAERO-CIMS. The condensation of the 44 µg m^{-3} of biomass-burning vapours took place within the first 4 h of the event, which is equivalent to a net condensation flux of 11 µg m^{-3} h^{-1}. From this flux and using the measured average particle condensation sink (180 h^{-1}), we can estimate the concentrations of condensing biomass-burning organic vapours to be equal to 61 ng m^{-3}, or 2.3×10^8 molecules cm^{-3} (assuming compounds have the same molecular weight as levoglucosan, 162 g mol^{-1}). The condensation of these vapours would result in a size-independent growth rate of ~11 nm h^{-1} (ref. [30]), which is on the same order as the average growth rates of sub-100 nm particles of ~19 nm h^{-1} measured during the NPG events. Thus, our calculations indicate that the condensation of supersaturated biomass smoke vapours is a plausible explanation for the observed organic-driven growth of sub-100 nm particles during the first hours of haze formation. We show that modest supersaturations in biomass-burning vapours of less than 0.1% of the total bbOA concentration are sufficient for explaining the observed growth. Once temperatures stabilize and emission rates balance loss rates, equilibrium can be reached within seconds and particles will no longer grow by the condensation of biomass-burning vapours. This appears to occur at ~21:00 (Fig. 4c).

We demonstrate through particle- size-resolved chemical information and time-series analysis that the organic fraction dominates the sub-100 nm particle growth. Chemical analysis of the organic vapours shows a stark increase in biomass-burning emissions and partitioning ratios during sub-100 nm particle growth. Through thermodynamic modelling, we show that the available bbOA vapours are able to grow particles across all sizes by 11 nm h^{-1}, which is comparable to the observed sub-100 nm particle growth of 19 nm h^{-1}. Taken together, the aerosol size-resolved chemical observations, the molecular analyses of organic vapours and the thermodynamic modelling provide strong evidence that organic vapours associated mainly with primary biomass-burning emissions are one of the key ingredients involved in the intense nocturnal particle growth during haze formation in Delhi.

Atmospheric implications

Intense nocturnal particle growth events occur systematically during the development of haze in the wider area of Delhi despite the low production rates of low-volatility vapours and their substantial loss under extremely polluted conditions. We show that the condensation of primary organic vapours from biomass burning leads to the intense growth of sub-100 nm particles into sizes relevant for haze formation. The sharp decrease in night-time temperatures and rapid increase in biomass-burning emissions result in a thermodynamic driving force that drives the condensation of these primary vapours into the particle phase.

Delhi's nocturnal particle growth events contrast sharply with observations at other urban locations around the world, in particular in Beijing, where secondary vapours formed through daytime photochemistry dominate particle formation and growth. At these locations, nocturnal changes in temperature and emission rates are probably less important in magnitude and speed than those observed in Delhi, which results in lower concentrations of supersaturated vapours to sustain nocturnal growth. In urban settings, such deviations from equilibrium are expected to occur on local scales near incomplete combustion emissions, where the cooling of concentrated organic vapours can rapidly generate primary particles. Furthermore, biomass burning for land clearing or from natural wildfires is a major global source of organic vapours in addition to directly emitted cloud condensation nuclei (CCN). These vapours can form an important, yet overlooked, driving force for nanoparticle growth towards CCN sizes, especially during the rapid cooling of vertically transported biomass-burning plumes. Further, nanoparticles are the most dangerous fraction of particulates owing to their deeper reach in the human body. With the increasing global importance of wildfires in a warmer atmosphere, we expect the condensation of biomass-burning vapours to have important effects for particle concentrations, size distributions and mixing states, hence influencing CCN concentrations and clouds on a global scale and human health on a local/regional scale.

Our results show that uncontrolled biomass burning not only is an important source for the total aerosol mass in Delhi but also contributes to the particle-number concentration by driving nocturnal particle growth. Using BC as the main tracer, we estimate that ~70% of the total particle-number concentration during the development of haze is not related to direct emissions (Extended Data Fig. 10a,b). Given that uncontrolled biomass burning for residential heating and cooking is rife in the IGP, we expect this growth mechanism to be a source of ultrafine particles (the most dangerous fraction of particulates owing to their deeper reach in the human body) in the entire region, affecting the health of 5% of the world's population and impacting the regional climate. Therefore, the reduction of uncontrolled combustion, especially during conducive weather conditions, may limit the amount of supersaturated vapours available for nanoparticle growth and hence may be an effective strategy for the mitigation of nocturnal particulate number during haze in Delhi.

Online content

Any methods, additional references, Nature Portfolio reporting summaries, source data, extended data, supplementary information, acknowledgements, peer review information; details of author contributions and competing interests; and statements of data and code availability are available at https://doi.org/10.1038/s41561-023-01138-x.

References

1. IQAir. World Air Quality Report. *2019 World Air Qual. Rep.* 1–35 (2019).
2. Beig, G. et al. Anatomy of the winter 2017 air quality emergency in Delhi. *Sci. Total Environ.* **681**, 305–311 (2019).
3. Kanawade, V. P. et al. What caused severe air pollution episode of November 2016 in New Delhi? *Atmos. Environ.* **222**, 117125 (2020).
4. Ravindra, K. et al. Real-time monitoring of air pollutants in seven cities of North India during crop residue burning and their relationship with meteorology and transboundary movement of air. *Sci. Total Environ.* **690**, 717–729 (2019).

5. Zhang, R., Khalizov, A., Wang, L., Hu, M. & Xu, W. Nucleation and growth of nanoparticles in the atmosphere. *Chem. Rev.* **112**, 1957–2011 (2012).
6. Zhang, R. et al. Formation of urban fine particulate matter. *Chem. Rev.* **115**, 3803–3855 (2015).
7. Kulmala, M., Kerminen, V. M., Petäjä, T., Ding, A. J. & Wang, L. Atmospheric gas-to-particle conversion: why NPF events are observed in megacities? *Faraday Discuss.* **200**, 271–288 (2017).
8. Yao, L. et al. Atmospheric new particle formation from sulfuric acid and amines in a Chinese megacity. *Science* **361**, 278–281 (2018).
9. Salimi, F., Rahman, M. M., Clifford, S., Ristovski, Z. & Morawska, L. Nocturnal new particle formation events in urban environments. *Atmos. Chem. Phys.* **17**, 521–530 (2017).
10. Kanawade, V. P. et al. Observations of new particle formation at two distinct Indian subcontinental urban locations. *Atmos. Environ.* **96**, 370–379 (2014).
11. Sebastian, M., Kanawade, V. P. & Pierce, J. R. Observation of sub-3 nm particles and new particle formation at an urban location in India. *Atmos. Environ.* **256**, 118460 (2021).
12. Gani, S. et al. Submicron aerosol composition in the world's most polluted megacity: the Delhi Aerosol Supersite study. *Atmos. Chem. Phys.* **19**, 6843–6859 (2019).
13. Tobler, A. et al. Chemical characterization of $PM_{2.5}$ and source apportionment of organic aerosol in New Delhi, India. *Sci. Total Environ.* **745**, 140924 (2020).
14. Gunthe, S. S. et al. Enhanced aerosol particle growth sustained by high continental chlorine emission in India. *Nat. Geosci.* https://doi.org/10.1038/s41561-020-00677-x (2021).
15. Ojha, N. et al. On the widespread enhancement in fine particulate matter across the Indo–Gangetic Plain towards winter. *Sci. Rep.* **10**, 5862 (2020).
16. Sembhi, H. et al. Post-monsoon air quality degradation across northern India: assessing the impact of policy-related shifts in timing and amount of crop residue burnt. *Environ. Res. Lett.* **15**, 104067 (2020).
17. Andreae, M. O. & Merlet, P. Emission of trace gases and aerosols from biomass burning. *Glob. Biogeochem. Cycles* **15**, 955–966 (2001).
18. Bruns, E. A. et al. Identification of significant precursor gases of secondary organic aerosols from residential wood combustion. *Sci. Rep.* **6**, 27881 (2016).
19. Lim, C. Y. et al. Secondary organic aerosol formation from the laboratory oxidation of biomass burning emissions. *Atmos. Chem. Phys.* **19**, 12797–12809 (2019).
20. Kodros, J. K. et al. Rapid dark aging of biomass burning as an overlooked source of oxidized organic aerosol. *Proc. Natl Acad. Sci. USA* **117**, 33028–33033 (2020).
21. Decker, Z. C. J. et al. Nighttime chemical transformation in biomass burning plumes: a box model analysis initialized with aircraft observations. *Environ. Sci. Technol.* **53**, 2529–2538 (2019).
22. Wei, Y. et al. Nocturnal $PM_{2.5}$ explosive growth dominates severe haze in the rural North China Plain. *Atmos. Res.* **242**, 105020 (2020).
23. Zhu, Y. et al. Comparative analysis of new particle formation events in less and severely polluted urban atmosphere. *Atmos. Environ.* **98**, 655–664 (2014).
24. An, J. et al. Characteristics of new particle formation events in Nanjing, China: effect of water-soluble ions. *Atmos. Environ.* **108**, 32–40 (2015).
25. Canagaratna, M. R. et al. Chemical and microphysical characterization of ambient aerosols with the aerodyne mass spectrometer. *Mass Spectrom. Rev.* **26**, 185–222 (2007).
26. Kulmala, M. et al. Is reducing new particle formation a plausible solution to mitigate particulate air pollution in Beijing and other Chinese megacities? *Faraday Discuss.* https://doi.org/10.1039/d0fd00078g (2021).
27. Chen, Y. et al. Ammonium chloride associated aerosol liquid water enhances haze in Delhi, India. *Environ. Sci. Technol.* https://doi.org/10.1021/acs.est.2c00650 (2022).
28. Xie, M., Hannigan, M. P. & Barsanti, K. C. Gas/particle partitioning of 2-methyltetrols and levoglucosan at an urban site in Denver. *Environ. Sci. Technol.* **48**, 2835–2842 (2014).
29. Wang, M. et al. Photo-oxidation of aromatic hydrocarbons produces low-volatility organic compounds. *Environ. Sci. Technol.* **54**, 7911–7921 (2020).
30. Nieminen, T., Lehtinen, K. E. J. & Kulmala, M. Sub-10 nm particle growth by vapor condensation—effects of vapor molecule size and particle thermal speed. *Atmos. Chem. Phys.* **10**, 9773–9779 (2010).

Suneeti Mishra[1], Sachchida Nand Tripathi[1] ✉, Vijay P. Kanawade[2], Sophie L. Haslett[3], Lubna Dada[4], Giancarlo Ciarelli[5], Varun Kumar[4,9], Atinderpal Singh[6,10], Deepika Bhattu[4,11], Neeraj Rastogi[6], Kaspar R. Daellenbach[4], Dilip Ganguly[7], Prashant Gargava[8], Jay G. Slowik[4], Markku Kulmala[5], Claudia Mohr[3], Imad El-Haddad[4] ✉ & Andre S. H. Prevot[4] ✉

[1]Department of Civil Engineering, Indian Institute of Technology Kanpur, Kanpur, India. [2]Centre for Earth, Ocean, and Atmospheric Sciences, University of Hyderabad, Hyderabad, India. [3]Department of Environmental Science, Stockholm University, Stockholm, Sweden. [4]Laboratory of Atmospheric Chemistry, Paul Scherrer Institute, Villigen, Switzerland. [5]Institute for Atmospheric and Earth System Research/Physics, University of Helsinki, Helsinki, Finland. [6]Geosciences Division, Physical Research Laboratory, Ahmedabad, India. [7]Centre for Atmospheric Sciences, Indian Institute of Technology Delhi, New Delhi, India. [8]Atmospheric Sciences, Centre for Pollution Control Board, Delhi, India. [9]Present address: Institut National de l'Environnement Industriel et des Risques (INERIS), Verneuil-en-Halatte, France. [10]Present address: Department of Environmental Studies, University of Delhi, Delhi, India. [11]Present address: Department of Civil and Infrastructure Engineering, Indian Institute of Technology Jodhpur, Jodhpur, India. ✉e-mail: snt@iitk.ac.in; imad.el-haddad@psi.ch; andre.prevot@psi.ch

Methods

Site information and measurement facility

We conducted measurements at the Department of Atmospheric Sciences, IITD (28.54° N, 77.19° E), Delhi. Instruments were deployed on the third floor of the building (~15 m above ground level). We performed measurements from 5 January to 10 February in 2019. Delhi is the capital city of India and has been one of the world's most polluted cities for the past few years[1]. The geography of this region also plays a vital role in pollutant accumulation within the boundary layer. Delhi lies in the western IGP, a foreland basin that developed adjacent to the Himalayan mountain belt. Delhi is a populated region (>12,000 people km^{-2} with a total area of 1,483 km^2) and is subjected to a myriad of anthropogenic pollution sources such as heavy traffic, thermal power plants, industry (clusters of metal-processing smelters and steel-pickling industries), rubber/plastic processing units and lead batteries, to name a few[13,31]. Thus, this region, which often experiences stable meteorological conditions and calm wind conditions, is loaded with heavy pollution every winter.

During the observation period, the average wind speed varied from 0.5 to 3.0 m s^{-1}, with a mean speed of 1.07 m s^{-1} during the night. The winds from northwest and southeast were more prevalent during the study period. An arterial road with high traffic intensity throughout the day and heavy diesel vehicles at night is north (~200 m) of the sampling site. An industrial estate (Okhla) is situated to the east of our sampling site. This area is around 9 km (aerial distance) from IITD and is an industrial hub that contributes to emissions from metal-processing (finishing and plating) industries, automobile industries and distilleries, to name a few. Delhi is situated in the IGP, which is also a global hotspot of ammonia (NH_3) due to intense agricultural activities, excessive fertilizer use and fertilizer production plants[32]. In addition, every year, the high biomass-burning emissions at the onset of winter (due to rice-stubble burning) transported from the upwind regions of Punjab and Haryana further worsen the air pollution scenario. Furthermore, comparatively stable atmospheric conditions (owing to its geography), abundant ammonia and continuous primary emissions into the atmosphere along with the already existing anthropogenic pollution and secondary OA precursors transform this region into an ideal open atmospheric chamber for such studies.

Instrumentation and data analysis

A suite of instruments was deployed for measuring the particle-number–size distribution, size-resolved chemical composition, trace gases, volatile organic carbon and meteorological parameters at the site. A scanning mobility particle sizer (GRIMMS SMPS, long differential mobility analyser) was used to scan the particles on the basis of their electrical mobility, and a butanol-based condensation particle counter (CPC model 5.416) was used to count the number of particles of that specific mobility. The particle-number–size distributions were measured at a flow rate of 0.3 l min^{-1} with 3 l min^{-1} sheath flow. The long differential mobility analyser was factory calibrated, and it measured size distribution in 45 bins from 19.97 nm to 999 nm. The dry fractions of the particle size distributions were measured at 5 min resolution in real time. The particle-number concentration was extracted by data inversion and was then corrected for diffusion losses and multiple charge correction. It was placed in tandem with an HR-ToF-AMS drawing ambient air from a PM_1 inlet (PM_1 cyclone is installed at the inlet of the sampling line to measure the particulate matter having an aerodynamic diameter less than or equal to 1 µm).

The Aerodyne HR-ToF-AMS[33–35] was used to measure the size-resolved chemical compositions of sub-micrometre particles at 2 min resolution. It was operated in the highly sensitive V mode, and all the required calibrations such as particle velocity, ionization efficiency and inlet flow were performed using well-known standard protocols[36]. The mass-based ionization-efficiency calibration was done using 300 nm ammonium nitrate particles, and the default relative ionisation efficiency mentioned elsewhere[25] were used for calculations. The detailed discussion on the instruments is fully characterized and validated in previous studies[37,38]. The composition-dependent collection efficiency[39] was used to calculate the final concentration[40]. Standard toolkits (SQUIRREL (Sequential Igor Data Retrieval) and PIKA (Peak Integration by Key Analysis) scripted in IGOR (Wavemetrics, Inc.) were used for high-resolution chemical analysis. Detailed description of the analysis has been discussed[38]. Since the lens transmission efficiency of HR-ToF-AMS is low for diameters less than 60 nm, the size-resolved chemical composition above 60 nm was used for analysis.

Gas monitors were also deployed to measure the trace gases CO, NO_x (Ecotech Serinus) and O_3 (model 205, 2B Technologies). For the measurement of BC, an online seven-wavelength dual-spot Aethalometer (AE33, Magee Scientific)[41] was used. Out of the seven wavelengths, the absorption coefficient at 880 nm was used to estimate the BC concentration, and the measured BC concentrations were corrected for filter loading and tape advancement error. The meteorological data were measured using the automated weather station at the same site, whereas the visibility data were obtained by India Meteorological Department (Palam Airport). The planetary boundary layer data were calculated by MERRA-2 (Modern-Era Retrospective Analysis for Research and Applications v.2) reanalysis[42].

To measure the gas-phase and particle-phase molecular compositions and compound-specific volatility information, a chemical ionization mass spectrometer fitted with a filter inlet for gases and aerosols (FIGAERO-CIMS, Aerodyne)[43] was deployed. The negative iodide ion (I^-) was used as a reagent, making the instrument highly sensitive to oxidized organic material. The FIGAERO inlet allows both gas- and particle-phase information to be collected semi-simultaneously. The gas phase was sampled directly through a ~2 m long, 1/4 inch inner-diameter inlet for approximately 20 min in every 90 min period. During the last 3 min of gas-phase sampling, particles were sampled onto a Teflon filter (PALL Zefluor, 2 µm pore size, 25 mm diameter) at a rate of 2 lpm. The filter was then placed in front of the CIMS inlet and heated over the course of 30 min to a temperature of 200 °C, at which it was held for 20 min before being cooled again to room temperature over 15 min. During the heating period, organic compounds desorb from the filter and enter the CIMS inlet, where they cluster with I^- and are then observed in the time-of-flight mass spectrometer. Each particle-phase data point is established by integrating the signal from the start of the heating to the start of the cooling phase, and each gas-phase data point by averaging across approximately 20 min of measurements, which yields approximately one data point every 90 min. Levoglucosan was observed in both the gas and the particle phase at AMU 289 ($I.C_6H_{10}O_5^-$).

The bulk aerosol water content was calculated by using AMS measurements to estimate the hygroscopic factor. This hygroscopic factor was then applied to each size bin in the SMPS measurements. The particles were then modelled to grow and alter the particle size distribution accordingly. The Zdanovskii, Stokes and Robinson mixing rule was used following the same method as described in the literature[44]. Comparisons in the literature show that AWC calculated using this technique agrees well with results from alternative approaches, including direct measurements of water content and the use of the ISORROPIA II, a thermodynamic equilibrium model[45]. In the Zdanovskii, Stokes and Robinson method, inorganic salt concentrations in the atmosphere are calculated by neutralizing the cation (NH_4^+) with the available anions (SO_4^{2-}, NO_3^-, Cl^- and HSO_4^-) using a simple ion-pairing scheme based on their stoichiometric concentrations and preferential reactivity[46]. Sulfate ions were assigned first to the neutral salt ammonium bisulfate (NH_4HSO_4), with additional ammonium ions being added to form ammonium sulfate ($(NH_4)_2SO_4$) if sufficient ion remained.

Particle growth-rate calculation

The particle growth rates were estimated by fitting the temporal variation of the particle-number mode diameter of the number distribution to a first-degree polynomial.

The condensation sink is calculated by

$$\mathrm{CS} = 2\pi \sum_{D_p} \beta(D_p) \times D_p \times N(D_p) \quad (1)$$

where $\beta(D_p)$ is the transitional correction factor (calculated according to the Fuchs–Sutugin equation[46]), D_p is the particle diameter and $N(D_p)$ is the particle-number concentration. For further calculations of coagulation sink, standard methods described previously[10,47] were applied. Size-resolved growth-rate[48] calculation is performed to assess the individual growth of particles in sizes of 25–40 nm, 40–60 nm, 60–100 nm and >100 nm (Supplementary Tables 1 and 2). The growth rates in these individual bins provide more information on how stable these particles are at higher diameter and, hence, further growth into bigger-diameter particles. The growth rates of chemical species (organics, nitrate, sulfate, ammonium and chloride) were also calculated with corresponding SMPS growth rates (Supplementary Table 3). The growth rates from this study were also compared with worldwide results (Supplementary Table 4).

For homogeneity and smooth comparison between the SMPS and AMS size distributions, the diameter used in this study is the mobility diameter (D_{mob}). The time- and composition-dependent particle density was calculated by the organics, sulfate, nitrate, ammonium, chloride and BC measured concentrations[49]. Assuming the atmospheric particles to be spherical, the aerodynamic diameter was then converted into mobility diameter[50].

Synthesis of Multilinear Engine-2 results from OAs

Source apportionment of OA mass spectra was performed using the PMF model[51]. The Multilinear Engine-2 algorithm was used to solve the PMF model using the Source Finder[52] (SoFi, Datalystica Ltd) interface version 6.6. To explore the rotational ambiguity, the a-value approach was used to constrain from known factor profiles and/or factor time series. An eight-factor solution was analysed and verified for environmental interpretability. A total of five OA factors were identified in the PMF analysis: HOA, bbOA-1, bbOA-2, LO-OOA and MO-OOA. Detailed discussion about the methodology and the factor solution has been published previously[38].

Gas-phase PMF

Source apportionment was performed on the gas-phase data from FIGAERO-CIMS. A six-factor solution was chosen as the best solution, yielding a rush hour/ traffic factor, two oxidation (daytime and residual) factors, one petrochemical vapour factor, one night-time biomass-burning factor and a background factor. A detailed discussion about the PMF and the factor selection will be covered in a separate paper (Haslett et al.[44]).

bbOA partitioning modelling using the volatility basis set

To calculate the partitioning of organic material between the gas and particle phases, we have used the 1.5-dimensional volatility basis set approach proposed by Koo et al.[53]. The model includes five volatility bins ranging from 10^{-1} to 10^{3} μg m^{-3} in saturation concentrations (C^*) and with molecular structures (weights) for each of the volatility bins retrieved from the group contribution approach used for the two-dimensional volatility basis set as well as the van Krevelen relation[54–56]. The dependence of C^* on temperature is described by the Clausius–Clapeyron equation[57]. An effective enthalpy of vaporization (ΔH) value of 35 kJ mol^{-1} is set for all the secondary OA species, whereas for primary biomass-burning emissions, ΔH is based on the following estimations retrieved from ref. [58]:

$$\Delta H = -4 \log\left(C^*_{298\mathrm{K}}\right) + 85 \mathrm{kJ\,mol}^{-1} \quad (2)$$

The model assumes that the equilibrium between the two phases is reached instantaneously, therefore neglecting kinetic limitations.

Individual cases (eight) were assumed for the model calculations to incorporate the entire range of atmospheric conditions to predict internally and externally mixed bbOA. For internally mixed calculations, we assume that HOA, LO-OOA and MO-OOA are added as additional pre-existing organic mass. The box model does not account for changes in partitioning as induced by changes in pH.

The eight cases for which the model predictions are calculated for all nocturnal growth events are the following:

Case 1: externally mixed bbOA, including temperature

Case 2: internally mixed bbOA, including temperature

Case 3: externally mixed bbOA including temperature and RH variations

Case 4: internally mixed bbOA including temperature and RH variations

Case 5 to Case 8: the same as Case 1 to Case 4 but at constant initial temperature

We have considered the organic and inorganic particles to be externally mixed as they show clearly two different particle populations based on the AMS particle time-of-flight measurements. However, we have considered the partitioning of compounds into the water related to the organic fraction.

Contribution of primary- and secondary-particle-source emissions to accumulation mode

The relative contribution of primary and secondary sources to the accumulation-mode particles was estimated by using the number concentration of primary particles using BC as the main tracer of traffic and other primary emissions. Detailed description of the method and its limitations is presented elsewhere[59]. The number concentration of primary particles is estimated using the relation:

$$N\_\mathrm{direct} = \mathrm{BC} \times S1 \quad (3)$$

where N_direct emissions is the estimated number of primary-accumulation-mode particles emitted by traffic and other sources, while $S1$ is the amount of primary-accumulation-mode particles emitted per microgram per cubic metre of BC and is derived semi-empirically from simultaneous observations of the accumulation-mode particles and BC. We computed the ratio of the total accumulation-mode number concentration to BC (N_total /BC) for all measurements and used the 0.1th, 0.5th, 1st, 1.5th, 2nd and 5th percentiles as $S1$ at different thresholds as shown in Extended Data Fig. 10a. We estimate the fraction of indirect emissions (shown in Extended Data Fig. 10b). The latter is calculated as follows:

$$N\_\mathrm{indirect} = N\_\mathrm{total} - N\_\mathrm{direct} \quad (4)$$

Here N_indirect is the number of accumulation-mode particles from indirect emissions, N_total is the total measured concentration of particles in the accumulation mode and N_direct is the number of accumulation-mode particles from traffic, calculated as described in the preceding. Our results show that the primary fraction of accumulation-mode particles is contributing up to 33% even at higher $\mathrm{PM}_{2.5}$ levels.

Data availability

All the data displayed in figures, including concentrations of particle-number concentration and NR-PM1 species measured by the HR-ToF-AMS in Delhi in this study, are available in the Figshare repository: https://doi.org/10.6084/m9.figshare.21932136. Source data are provided with this paper.

Code availability

Codes for the thermodynamic modelling conducting the analysis presented here can be obtained upon request from the corresponding author.

References

31. Rai, P. et al. Real-time measurement and source apportionment of elements in Delhi's atmosphere. *Sci. Total Environ.* **742**, 140332 (2020).
32. Kuttippurath, J. et al. Record high levels of atmospheric ammonia over India: spatial and temporal analyses. *Sci. Total Environ.* **740**, 139986 (2020).
33. Aiken, A. C. et al. Mexico City aerosol analysis during MILAGRO using high resolution aerosol mass spectrometry at the urban supersite (T0)—part 1: fine particle composition and organic source apportionment. *Atmos. Chem. Phys.* **9**, 6633–6653 (2009).
34. Allan, J. D. et al. A generalised method for the extraction of chemically resolved mass spectra from Aerodyne aerosol mass spectrometer data. *J. Aerosol Sci.* **35**, 909–922 (2004).
35. Canagaratna, M. R. et al. Elemental ratio measurements of organic compounds using aerosol mass spectrometry: characterization, improved calibration, and implications. *Atmos. Chem. Phys.* **15**, 253–272 (2015).
36. Jayne, J. T. et al. Development of an aerosol mass spectrometer for size and composition analysis of submicron particles. *Aerosol Sci. Technol.* **33**, 49–70 (2000).
37. Kumar, V. et al. Highly time-resolved chemical speciation and source apportionment of organic aerosol components in Delhi, India, using extractive electrospray ionization mass spectrometry. *Atmos. Chem. Phys.* **22**, 7739–7761 (2022).
38. Singh, A. et al. Sources and characteristics of light-absorbing fine particulates over Delhi through the synergy of real-time optical and chemical measurements. *Atmos. Environ.* **252**, 118338 (2021).
39. Lalchandani, V. et al. Real-time characterization and source apportionment of fine particulate matter in the Delhi megacity area during late winter. *Sci. Total Environ.* **770**, 145324 (2021).
40. Middlebrook, A. M., Bahreini, R., Jimenez, J. L. & Canagaratna, M. R. Evaluation of composition-dependent collection efficiencies for the Aerodyne aerosol mass spectrometer using field data. *Aerosol Sci. Technol.* **46**, 258–271 (2012).
41. Drinovec, L. et al. The 'dual-spot' Aethalometer: an improved measurement of aerosol black carbon with real-time loading compensation. *Atmos. Meas. Tech.* **8**, 1965–1979 (2015).
42. Molod, A., Takacs, L., Suarez, M. & Bacmeister, J. Development of the GEOS-5 atmospheric general circulation model: evolution from MERRA to MERRA2. *Geosci. Model Dev.* **8**, 1339–1356 (2015).
43. Lopez-Hilfiker, F. D. et al. A novel method for online analysis of gas and particle composition: description and evaluation of a filter inlet for gases and AEROsols (FIGAERO). *Atmos. Meas. Tech.* **7**, 983–1001 (2014).
44. Haslett, S. L. et al. The radiative impact of out-of-cloud aerosol hygroscopic growth during the summer monsoon in southern West Africa. *Atmos. Chem. Phys.* **19**, 1505–1520 (2019).
45. Shen, X. J. et al. Variations in submicron aerosol liquid water content and the contribution of chemical components during heavy aerosol pollution episodes in winter in Beijing. *Sci. Total Environ.* **693**, 133521 (2019).
46. Fuchs, N. A. & Sutugin, A. G. in *Topics in Current Aerosol Research* (eds Hidy, G. M. & Brock, J. R.) 1–60 (Pergamon, 1971).
47. Dal Maso, M. et al. Formation and growth of fresh atmospheric aerosols: eight years of aerosol size distribution data from SMEAR II, Hyytiälä, Finland. *Boreal Environ. Res.* **10**, 323–336 (2005).
48. Hussein, T. et al. Observation of regional new particle formation in the urban atmosphere. *Tellus B* **60**, 509–521 (2008).
49. Zhou, Y. et al. Variation of size-segregated particle number concentrations in wintertime Beijing. *Atmos. Chem. Phys.* **20**, 1201–1216 (2020).
50. DeCarlo, P. F., Slowik, J. G., Worsnop, D. R., Davidovits, P. & Jimenez, J. L. Particle morphology and density characterization by combined mobility and aerodynamic diameter measurements. Part 1: theory. *Aerosol Sci. Technol.* **38**, 1185–1205 (2004).
51. Paatero, P. The Multilinear Engine—a table-driven, least squares program for solving multilinear problems, including the *n*-Way Parallel Factor Analysis Model. *J. Comput. Graph. Stat.* **8**, 854–888 (1999).
52. Canonaco, F., Crippa, M., Slowik, J. G., Baltensperger, U. & Prévôt, A. S. H. SoFi, an IGOR-based interface for the efficient use of the generalized Multilinear Engine (ME-2) for the source apportionment: ME-2 application to aerosol mass spectrometer data. *Atmos. Meas. Tech.* **6**, 3649–3661 (2013).
53. Koo, B., Knipping, E. & Yarwood, G. 1.5-Dimensional volatility basis set approach for modeling organic aerosol in CAMx and CMAQ. *Atmos. Environ.* **95**, 158–164 (2014).
54. Donahue, N. M., Epstein, S. A., Pandis, S. N. & Robinson, A. L. A two-dimensional volatility basis set: 1. Organic-aerosol mixing thermodynamics. *Atmos. Chem. Phys.* **11**, 3303–3318 (2011).
55. Donahue, N. M., Kroll, J. H., Pandis, S. N. & Robinson, A. L. A two-dimensional volatility basis set—Part 2: diagnostics of organic-aerosol evolution. *Atmos. Chem. Phys.* **12**, 615–634 (2012).
56. Donahue, N. M. et al. Aging of biogenic secondary organic aerosol via gas-phase OH radical reactions. *Proc. Natl Acad. Sci. USA* **109**, 13503–13508 (2012).
57. Sheehan, P. E. & Bowman, F. M. Estimated effects of composition on secondary organic aerosol mass concentrations. *Environ. Sci. Technol.* **35**, 2129–2135 (2001).
58. May, A. A. et al. Gas-particle partitioning of primary organic aerosol emissions: 3. Biomass burning. *J. Geophys. Res. Atmos.* **118**, 11327–11338 (2013).
59. Kulmala, M. et al. On the mode-segregated aerosol particle number concentration load: contributions of primary and secondary particles in Hyytiälä and Nanjing. *Boreal Environ. Res.* **21**, 319–331 (2016).

Acknowledgements

We thank the Central Pollution Control Board (CPCB), Government of India, for providing financial support for this experiment. S.N.T. gratefully acknowledges their support in conducting this research under grant no. AQM/Source apportionment_EPC Project/2017. S.M. and S.N.T. also acknowledge financial support received under Centre of Excellence Advanced Technologies for Monitoring Air-quality iNdicators (ATMAN) approved by PSA office, Government of India and supported by a group of philanthropic funders, including the Bloomberg Philanthropies, the Children's Investment Fund Foundation (CIFF), the Open Philanthropy and the Clean Air Fund. A.S.H.P. acknowledges the following project: the SDC Clean Air Project in India (grant no. 7F-10093.01.04). M.K. acknowledges ACCC Flagship funded by the Academy of Finland grant number 337549, Academy professorship funded by the Academy of Finland (grant no. 302958), Academy of Finland projects no. 1325656, 316114 and 325647, 'Quantifying carbon sink, CarbonSink+ and their interaction with air quality' INAR project funded by Jane and Aatos Erkko Foundation, European Research Council (ERC) project ATM-GTP contract no. 742206. G.C. acknowledges the support of the European Research Council with the project CHAPAs no. 850614. V.P.K. acknowledges support by the Department of Science & Technology (DST)-Science Engineering Research Board (SERB; ECR/2016/001333) and DST-Climate Change Division Program (Aerosol/89/2017). S.N.T. acknowledges the support of India Meteorological department (IMD, New Delhi) for providing visibility data. K.R.D. acknowledges support by the Swiss National Science Foundation Ambizione grant PZPGP2_201992.

Author contributions

S.N.T. and A.S.H.P conceptualized, designed, and planned the experiments. S.M., V.K., J.G.S., S.L.H. and A.S. prepared the measurement facility and handled instrumentation and data collection. S.M., V.K., S.L.H., V.P.K., L.D., C.M., and I.E.-H. analysed the data. I.E.-H. and G.C. performed modelling. S.N.T., A.S.H.P, M.K., I.E-H., C.M., N.R., D.B., K.R.D., D.G. and P.G. contributed to the scientific discussion. S.M. led the paper writing with specific inputs and edits from I.E.-H., C.M., S.N.T., and V.P.K. All co-authors reviewed and commented on the paper.

Competing interests

The authors declare no competing interests.

Additional information

Extended data is available for this paper at https://doi.org/10.1038/s41561-023-01138-x.

Supplementary information The online version contains supplementary material available at https://doi.org/10.1038/s41561-023-01138-x.

Correspondence and requests for materials should be addressed to Sachchida Nand Tripathi, Imad El-Haddad or Andre S. H. Prevot.

Peer review information *Nature Geoscience* thanks the anonymous reviewers for their contribution to the peer review of this work. Primary Handling Editor: Xujia Jiang, in collaboration with the *Nature Geoscience* team.

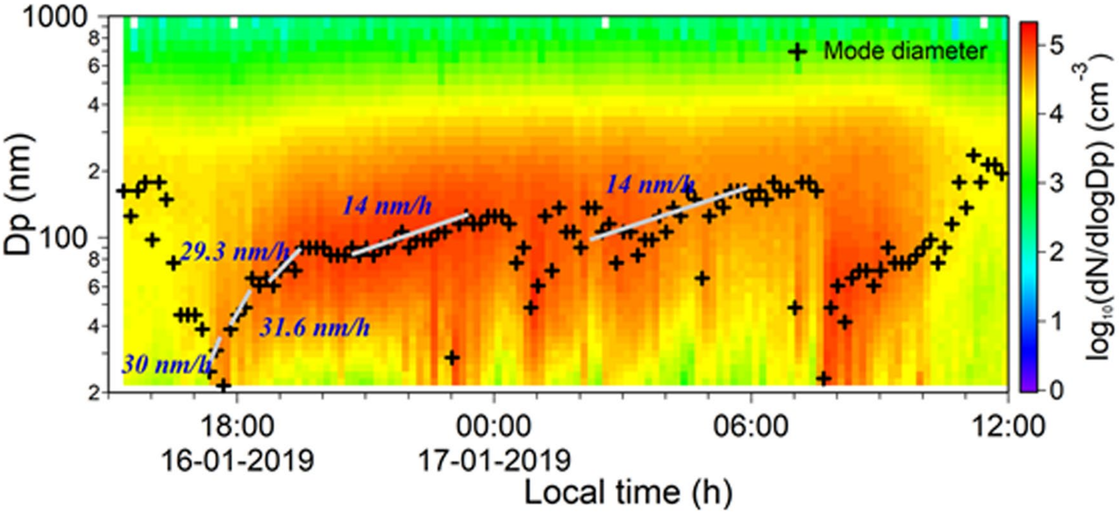

Extended Data Fig. 1 | A classical event. A typical particle nocturnal growth event of 16th January 2019 (one of the 27 growth event days).

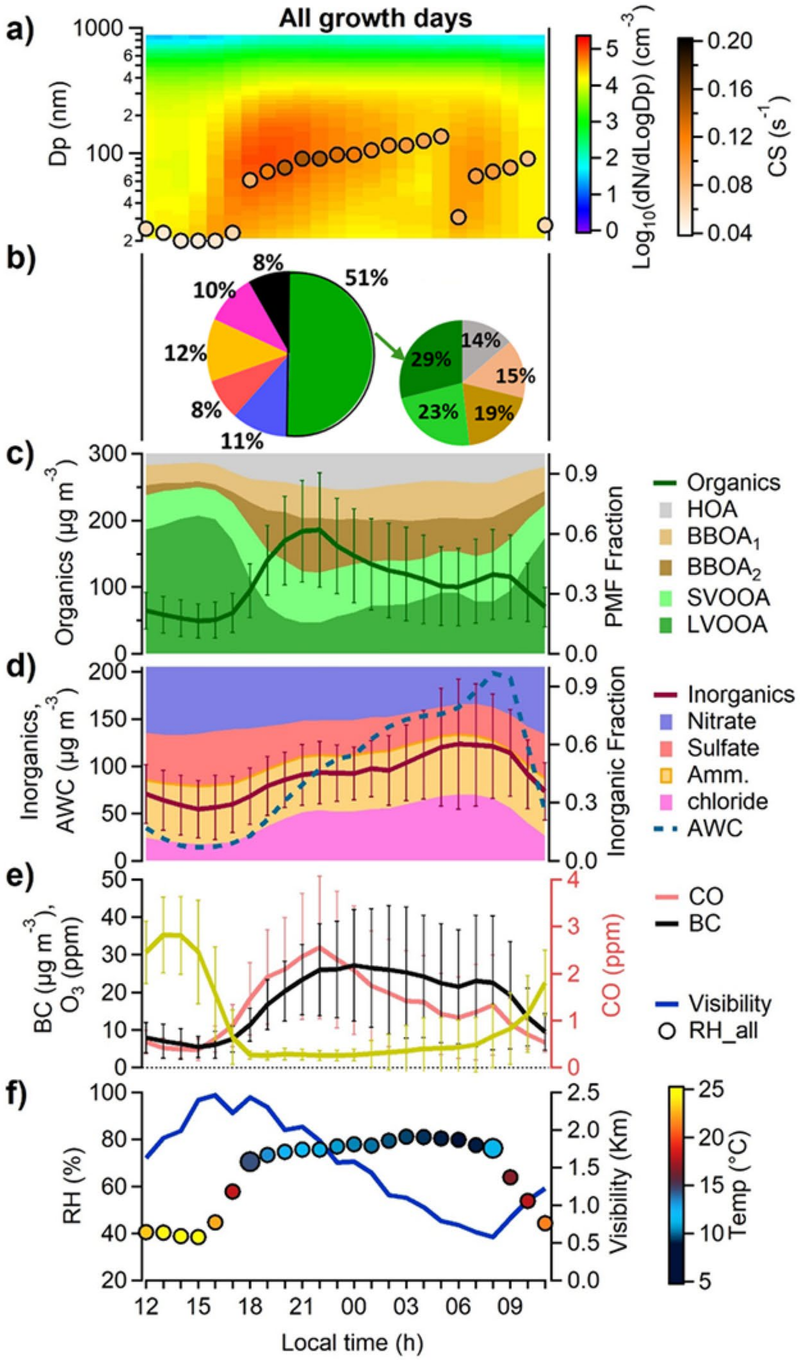

Extended Data Fig. 2 | Characteristics of all growth days. a) Average number size distribution for all NPG days along with their mode variation, color-coded with their respective condensation-sink values, **b**) fractional contributions to total PM1 and organic factors alone, **c**) diel variation of organics (mean ±1σ) (left) and stacked variation of organic factors (right), **d**) diel variation of inorganics (mean ±1σ) and aerosol water content (AWC) (left) and stacked variation of nitrate, sulphate, ammonium, and chloride (right), **e**) black carbon ((mean ± 1σ) and carbon monoxide, **f**) RH, temperature and visibility. The line and the error bars represent the mean and ±1 s.d. (n Number=27).

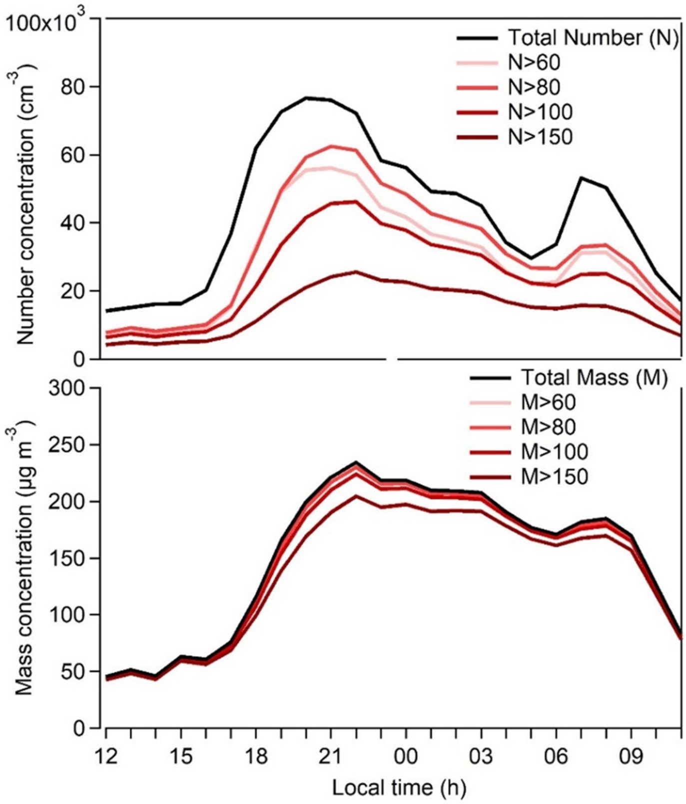

Extended Data Fig. 3 | Particle mass and Number variation. Diurnal variation of size-segregated particle number and mass concentrations on NPG event days.

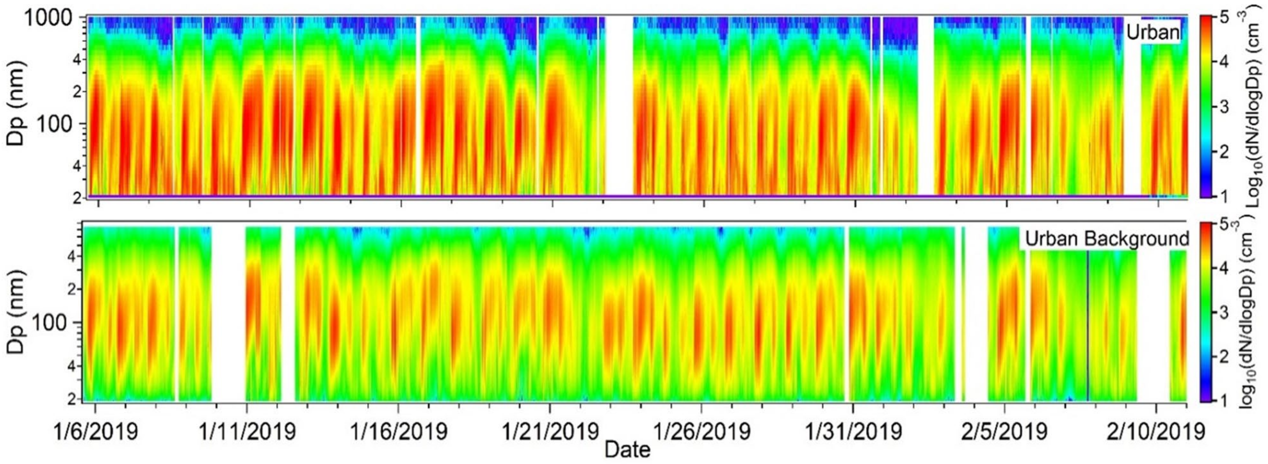

Extended Data Fig. 4 | Regionality of all growth days. Time-evolution of particle number-size distributions measured at urban (IITD) and at a sub-urban industrial (MRIU) location during January-February 2019. The urban background site (MRIU) is 20 Km downwind of our site.

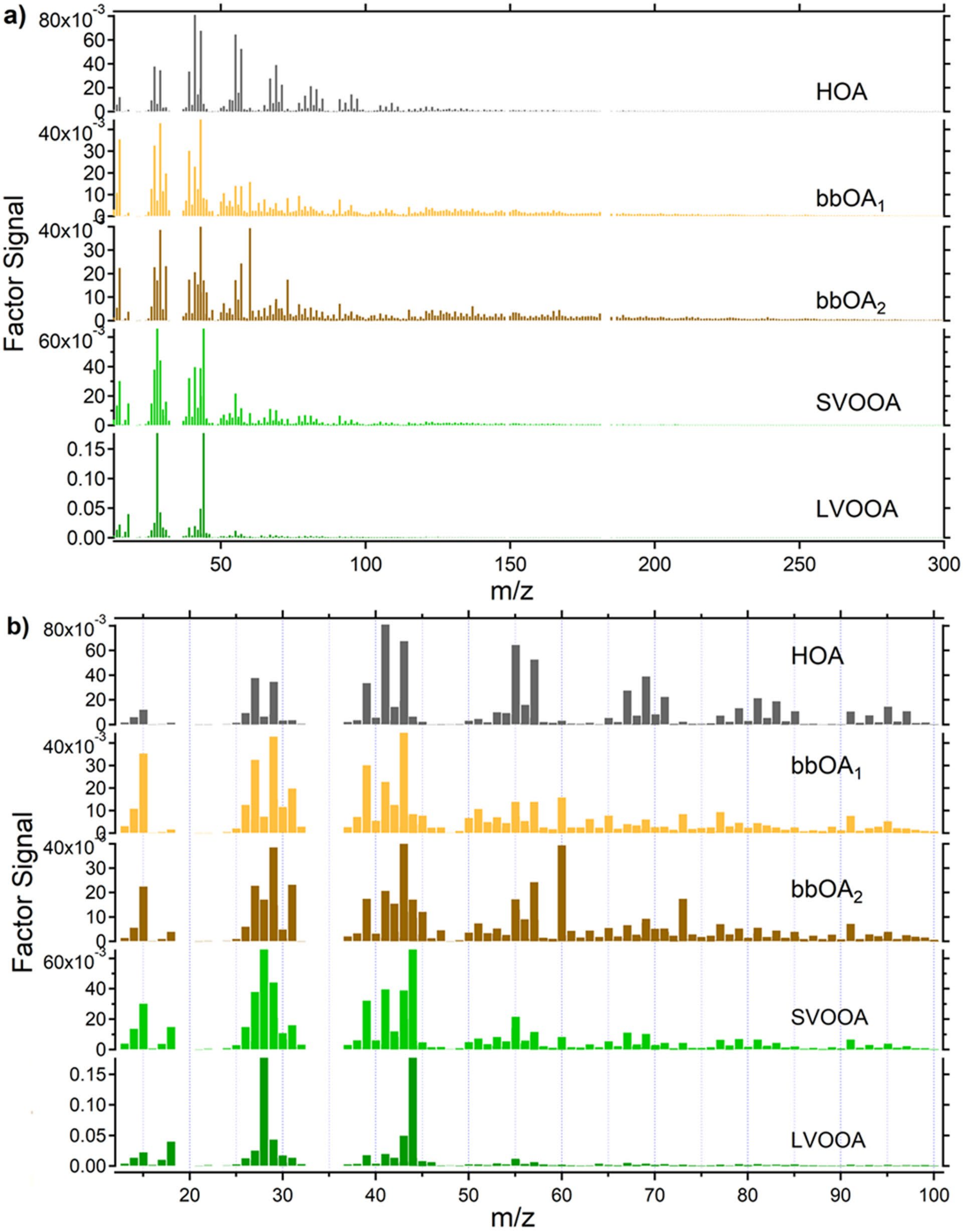

Extended Data Fig. 5 | OA-PMF factor solutions. a) PMF factor signals for the 5-factor solution, **b**) factor signals up to m/z 100.

https://doi.org/10.1038/s41561-023-01138-x

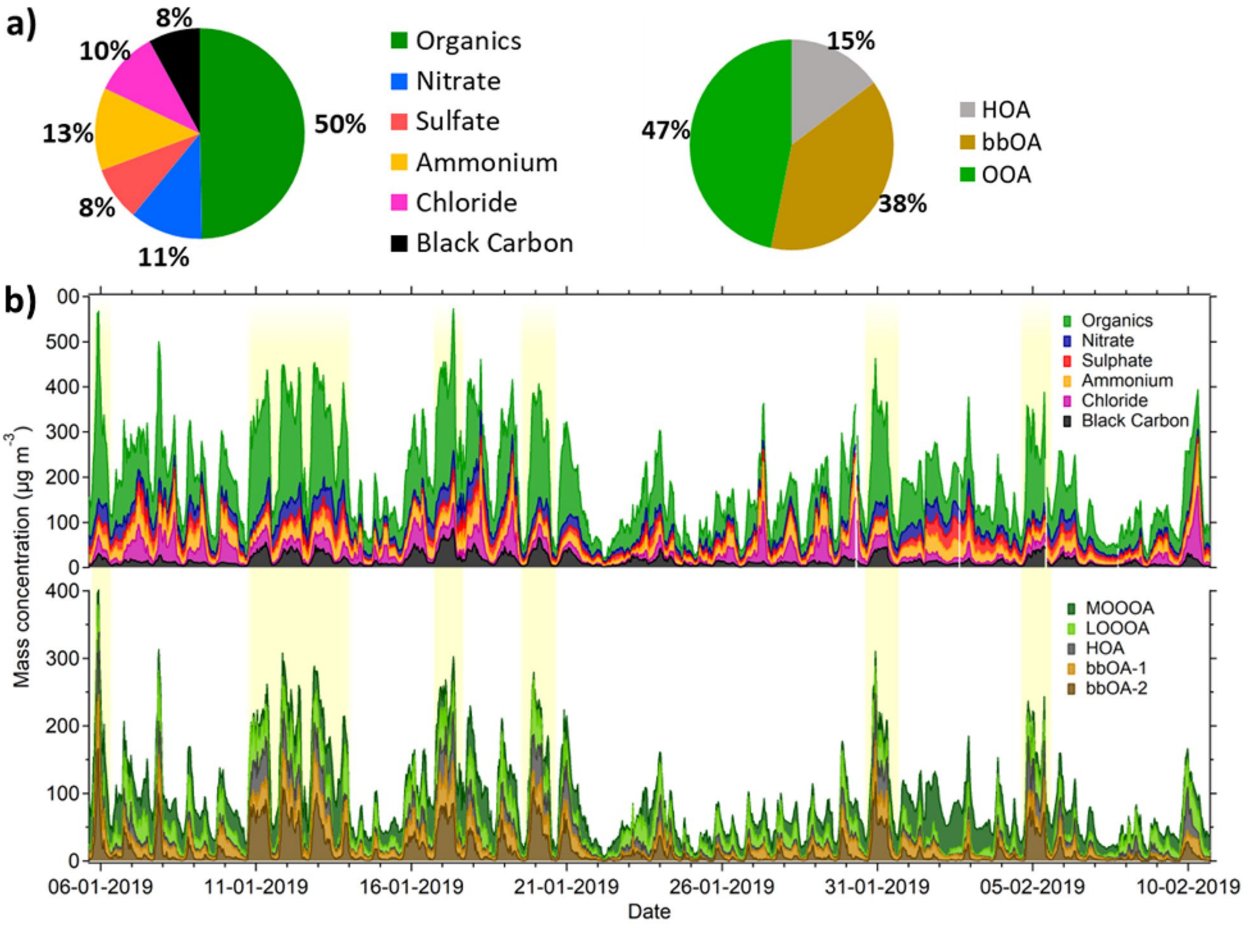

Extended Data Fig. 6 | OA-PMF contribution and variation. **a**) Fractional aerosol contribution of total PM1 and organic factors from HR-ToF-AMS PMF during the study period, **b**) time series of chemical species and organic factors, with elevated nocturnal growth days highlighted.

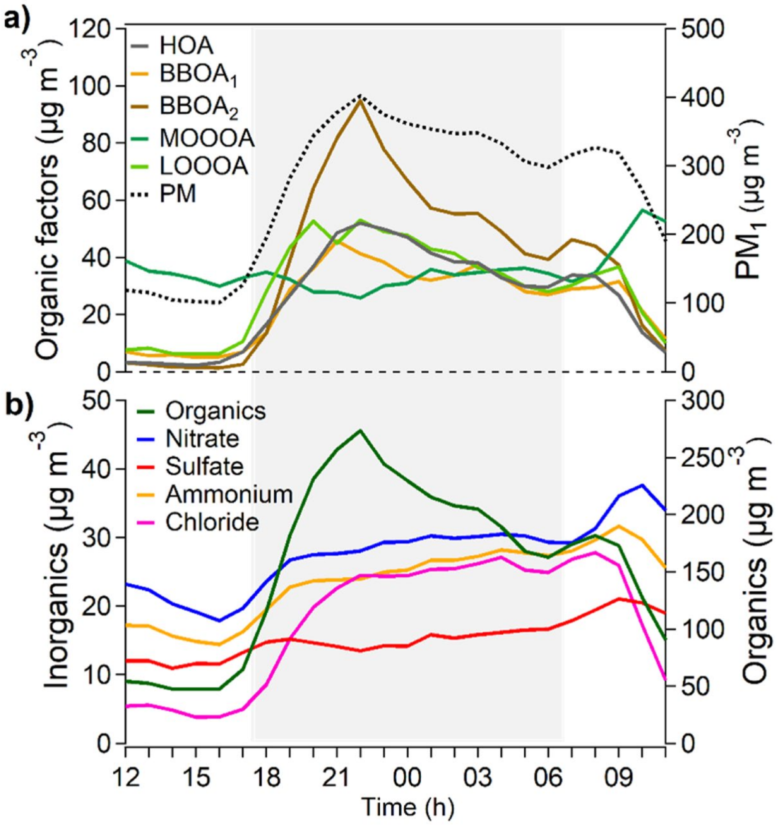

Extended Data Fig. 7 | OA-PMF factors variation. a) OA-PMF factors along with PM1 variation **b**) chemical species (organics, nitrate, ammonium, sulphate and chloride) during the NPG events.

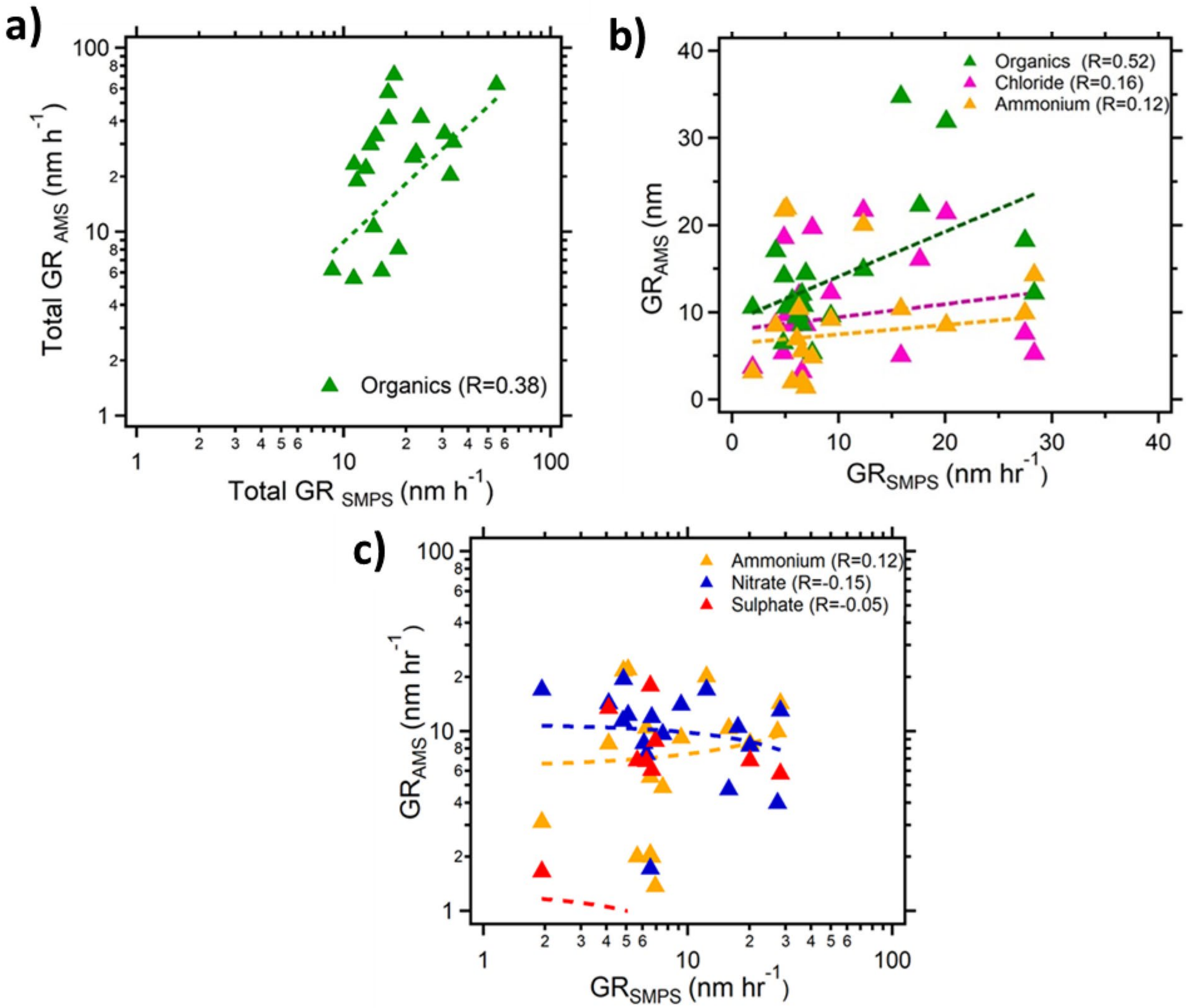

Extended Data Fig. 8 | GR correlation. Correlation of **a**) total growth rates of organics from HR-ToF-AMS to SMPS growth rates, **b**) scatter plot of growth rate from SMPS data (GRSMPS > 100 nm), and the corresponding growth rate of organics, ammonium and chloride from HR-ToF-AMS data (GRAMS > 100 nm), **c**) scatter plot of growth rates (GRSMPS > 100 nm) of secondary inorganics from HR-ToF-AMS to SMPS growth rates for all growth events, b, c) The lines indicate the slope of fit of each species.

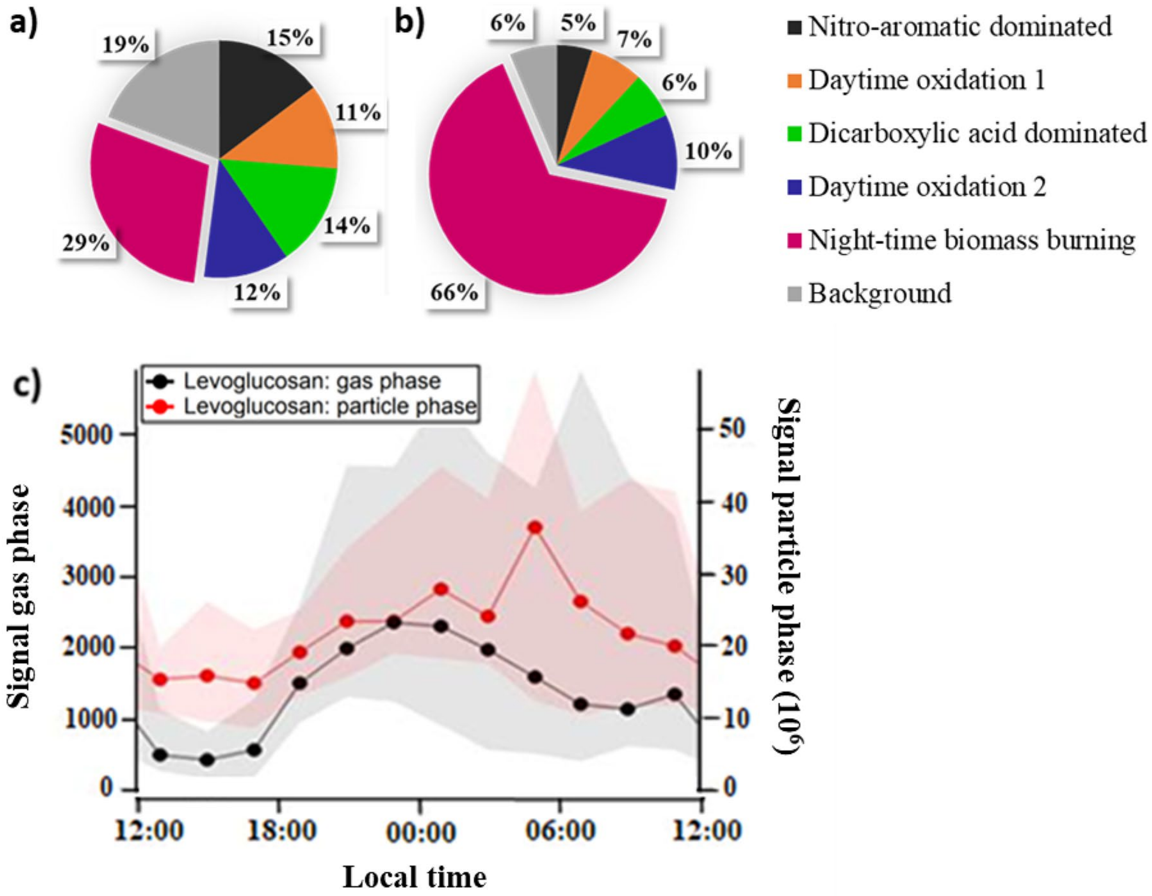

Extended Data Fig. 9 | Gas-phase PMF results. a,**b**) Fractional contribution of the gas-phase PMF factors during the entire study period (**a**) and on the NPG days (**b**). **c**) Diel variation of the levoglucosan signal in the gas phase and particle phase.

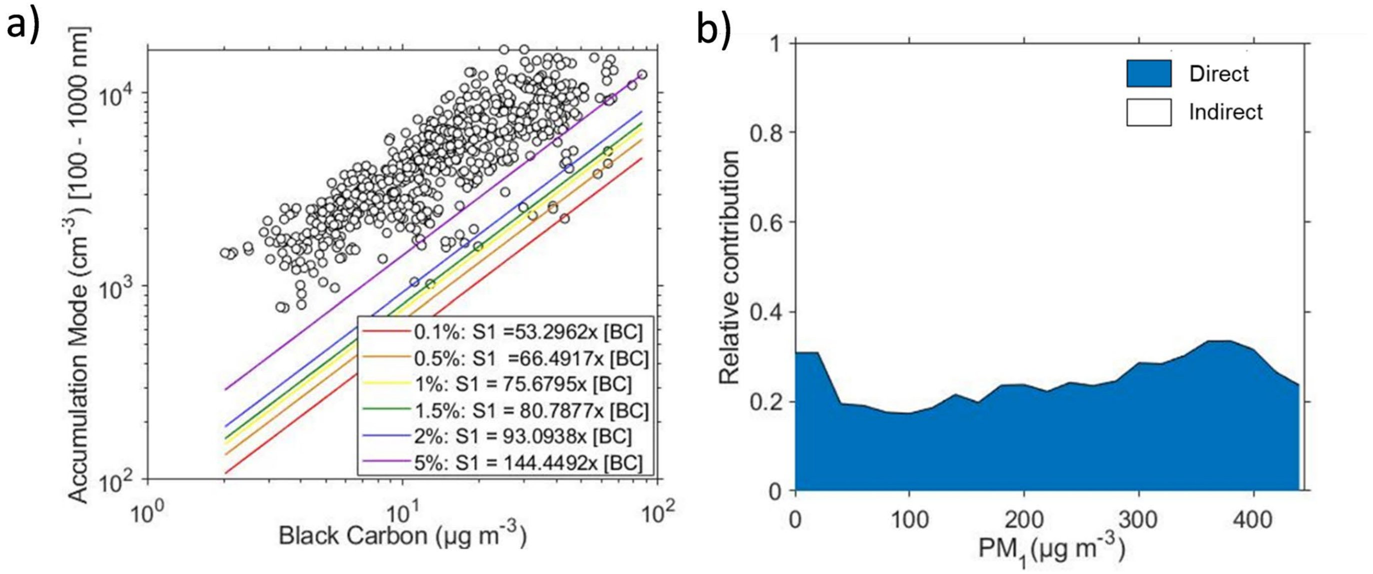

Extended Data Fig. 10 | Relative contribution. a) Accumulation mode concentration for all the NPG days as a function of the BC concentration, in the constrained fittings, **b**) The fraction of primary particles in the accumulation mode (>100 nm) estimated using the BC tracer method (Methods).